Energy transfer in $(PEA)_2FA_{n-1}Pb_nBr_{3n+1}$ quasi-2D perovskites

Journal Name

Energy transfer in $(PEA)_2FA_{n-1}Pb_nBr_{3n+1}$ quasi-2D perovskites

Džiugas Litvinas,[a] Ramūnas Aleksiejūnas,[*a] Patrik Ščajev,[a] Paulius Baronas,[a] Vaiva Soriūtė,[a] Chuanjiang Qin,[b] Takashi Fujihara,[c] Toshinori Matsushima,[d,e,f] Chihaya Adachi,[d,e,f] and Saulius Juršėnas[a]

Quasi-two dimensional perovskites demonstrate unique excitonic properties due to multilayer structure making them attractive for various optoelectronic applications. However, the thickness of individual perovskite sheets in wet cast quasi-2D layers tend to randomly fluctuate giving rise to specific type of disorder, which impact to carrier dynamics is rather complex and remains understudied. Here, we present a study of carrier transport in Ruddlesden–Popper type $(PEA)_2FA_{n-1}Pb_nBr_{3n+1}$ layers of order n from one to four, and in the bulk $FAPbBr_3$ layer. We use light induced transient grating technique to directly measure the carrier diffusion coefficient, and transient absorption with photoluminescence to investigate the energy relaxation pathways. We observe two distinct energy transfer processes on different time scales. Fast energy funnelling in thicker ($n \geq 3$) layers is observed up to 10 ps after excitation; we attribute it to short-distance transfer of excitons to neighbouring perovskite sheets of higher order. On the longer timescale of hundreds of picoseconds, carrier in-plane transport is governed by exciton diffusion in $n = 1$ and 2 layers and by free carrier plasma in thicker ones. Within the carrier density range of $(0.5-4) \times 10^{19}$ cm^{-3}, exciton diffusion coefficient in $n = 1, 2$ slowly increases from 1 to 2.8 cm^2/s, while in thicker layers the dependence is much stronger and diffusivity grows from 0.09 to 1.9 cm^2/s. We explain these dependencies by higher structural order in the thinner samples and stronger localization of carriers in thicker ones. Also, amplified spontaneous emission (ASE) is observed in thicker ($n \geq 3$) layers in electron-hole plasma, as evidenced by the typical ASE line redshift with excitation.

1 Introduction

Two-dimensional (2D) perovskites are intensively studied as an alternative for three-dimensional (3D) ABX_3 type perovskites for light-harvesting and light-emitting devices[1–3]. The main attractiveness of 2D perovskites lies in much higher environmental and

[a] Institute of Photonics and Nanotechnology, Faculty of Physics, Vilnius University, Sauletekio Ave. 3, LT-10257, Vilnius, Lithuania.

[*] E-mail: ramunas.aleksiejunas@ff.vu.lt.

[b] State Key Laboratory of Polymer Physics and Chemistry, Changchun Institute of Applied Chemistry (CIAC), Chinese Academy of Science, 5625 Renmin Street, Changchun 130022, China.

[c] Innovative Organic Device Laboratory, Institute of Systems, Information Technologies and Nanotechnologies (ISIT), Fukuoka Industry-Academia Symphonicity (FiaS) 2-110, 4-1 Kyudai-shinmachi, Nishi, Fukuoka 819-0388, Japan.

[d] International Institute for Carbon-Neutral Energy Research (WPI-I2CNER), Kyushu University, 744 Motooka, Nishi, Fukuoka 819-0395, Japan.

[e] Center for Organic Photonics and Electronics Research (OPERA), Kyushu University, 744 Motooka, Nishi, Fukuoka 819-0395, Japan.

[f] Adachi Molecular Exciton Engineering Project, Japan Science and Technology Agency (JST), ERATO, 744 Motooka, Nishi, Fukuoka 819-0395, Japan.

photo stability if compared to their 3D counterparts[4,5]. Also, the possibility to replace toxic Pb by Sn in single layer perovskites was demonstrated[6]. 2D perovskite solar cells with conversion efficiency above 12%[7] or mixed structures of 2D/3D perovskites with efficiency above 18%[8] were demonstrated with much improved resilience to environmental influence. In the last few years, 2D perovskites greatly advanced in light emission applications as well. Efficiency of 2D perovskite-based LEDs has already reached 20%[3], and stable CW lasing was demonstrated in 2D lead halide-based quasi-2D perovskite films[9]. Also, these materials show a number of unique properties that make them an interesting object for fundamental studies. Perhaps the most important one is very strong quantum and dielectric confinement of charge carriers leading to exciton binding energies as high as 490 meV[10]. The dielectric confinement is defined by the dielectric constant of organic molecules that make spacers between the sheets of perovskite octahedra; this grants rich possibilities to control excitonic properties by selecting different organic cation molecules[11]. Strongly bound excitons do not dissociate at rele-

vant temperatures and carrier densities, thus an excitonic nature of optical and electrical properties is prominent [1,12]. However, all these novel properties of 2D perovskites come together with even higher complexity. For instance, additional disorder arises from the intermixing of layers of slightly different thickness.

The most popular Ruddlesden–Popper type 2D perovskites can be described by a general chemical formula $(RNH_3)_2A_{n-1}M_nX_{3n+1}$, where RNH_3 is a large cation that serves as a barrier between quantum wells, A is a monovalent organic cation, M is a divalent metal cation, X is a halide anion, and n is a number of $[MX_6]^{4-}$ octahedral layers within a single quantum well. n is often referred to as the order of the perovskite layer and is one of the main parameters defining layer properties; e.g., the perovskites with $n \geq 2$ are not strictly two-dimensional and thus are called quasi-2D perovskites. One important trait of wet-cast quasi-2D perovskite layers is that they consist of many spacer-separated sheets of slightly different thickness (and order) fluctuating around some average value $< n >$ [13]. Different carrier confinement in neighbouring sheets results in varying potential landscape, which gives rise to fast energy transfer (funnelling) from thinner to thicker perovskite sheets in quasi-2D perovskite layers [14,15].

Carrier transport properties are known to be of crucial importance for the performance of perovskite devices [16,17]; therefore, it is imperative to understand how this complex potential landscape impacts carrier transport in quasi-2D perovskites. Diffusion coefficient (D) is the parameter well suited to quantify the efficiency of carrier transport in a material. D is also a key factor defining the efficiency of optoelectronic semiconductor devices like solar cells or LEDs, and enters as a parameter in drift-diffusion equations used for modelling of LEDs and diodes. Carrier transport has been extensively studied in 3D perovskites (see e.g. a perspective paper by L. Herz [18]); in particular, it has been shown that a fluctuating potential landscape causes carrier localization effects that brake the proportionality between carrier diffusivity and mobility, resulting in a strong dependence of D on carrier density N [19–21]. Carrier transport in quasi-2D perovskite layers is expected to become even more complex. This point can be illustrated by large dispersion of reported D values. For example, C. Zhou et al. obtained D values of 53.6 cm^2/s for exfoliated $(BA)_2PbI_4$ nano-platelets by local time-resolved photoluminescence technique [22]. On the other hand, M. Seitz et. al. obtained $D = 0.19$ cm^2/s in $(PEA)_2PbI_4$ by transient photoluminescence measurements [23]. Transient terahertz spectroscopy provided carrier mobility of $\mu = 17.4$ cm^2/(Vs), which results in $D = 0.45$ cm^2/s at room temperature [24]. While this discrepancy in values may be related to different measurement methods, it is also very likely that carrier transport is sensitive to the varying potential landscape. This assumption is confirmed by finding that changing the spacer molecule changes D value (measured under same conditions and with same technique) by an order of magnitude [23]. Therefore, it is imperative to find out what processes govern carrier transport in these materials.

Here, we address this problem by investigating carrier transport and its relation to energy funnelling in quasi-2D $(PEA)_2FA_{n-1}Pb_nBr_{3n+1}$ layers of orders $n = 1, 2, 3$ and 4 (by la-

belling the order with n we have in mind an average order, as discussed). $(PEA)_2FA_{n-1}Pb_nBr_{3n+1}$ is a promising 2D perovskite for green-emitting LEDs, where efficiencies above 18% have already been demonstrated [25]. We employ light induced transient grating (LITG) technique to measure D as a function of carrier density in the layers in all-optical way. This method is attractive as it allows for direct determination of diffusion coefficient and lifetime of carriers without need for electrical contacts [26]. Among other advantages, we would like to draw attention to the possibility of precise calibration of carrier density N under optical excitation from material absorption coefficient, which in turn enables measurement of $D(N)$ up to very high excitations relevant for high power light-emitting devices. Due to these reasons, LITG has been used for diffusion coefficient measurements in bulk perovskite crystals and thick layers, by our and other groups alike [20,21,27–30]. In this work, we combine this technique with transient photoluminescence (TPL) and absorption (TA) measurements to analyze the energy and carrier transport in highly excited quasi-2D perovskite layers at high excitations near the threshold of amplified spontaneous emission (ASE). We observe the energy transfer on two different time scales: one within first picosecond and the second within hundreds of picoseconds. We provide experimental evidence confirming that the fast process is related to exciton transition to higher n perovskite sheets where excitons dissociate either due to high carrier densities, or under influence of grain boundaries. We show that the latter process is crucial for ASE emergence. The slower transport process is related to lateral charge diffusion within the sheets. We observe a different dependence of $D(N)$ on n from those reported for iodide quasi-2D perovskites, diffusivity being higher in thinner samples. We discuss these results in a framework of different disorder of the layers that governs the carrier dynamics in the samples.

2 Experimental

2.1 Materials

Samples were fabricated by spin coating on quartz substrates. Before use, the substrates were first cleaned by ultrasonication and then irradiated by UV light. The precursor solution was made by dissolving formamidinium bromide (FABr), lead (II) bromide ($PbBr_2$) and phenethylamonium bromide ($PEABr_2$) in dimethyl-sulphoxide (DMSO). The resulting solution was filtered through a 0.45 μm membrane filter, then cast on a substrate spinning at a rate of 6000rpm over the course of 30s. The solution was allowed to crystallize at room temperature forming a perovskite layer. The layers were additionally encapsulated from ambient oxygen and humidity. The resulting stoichiometric formula of the nanolayers present in the samples was $(PEA)_2FA_{n-1}Pb_nBr_{3n+1}$.

2.2 Techniques

The main results of this paper have been obtained by using three time-resolved measurement techniques: transient absorption, photoluminescence, and light-induced transient gratings. All described measurements were performed at room temperature.

Transient absorption measurements were performed using

the setup made by "Light Conversion". The pulses from the Yb:KGW laser "PHAROS" (190 fs, 1030 nm) were split 95%/5% to form the pump and probe pulses. The wavelength of pump pulses was fine-tuned within 350–370 nm using the "ORPHEUS" optical parametric amplifier and "LYRA" second harmonic generator. The intensity of pump beam was controlled by a gradient mirror. These pulses were directed into the "Harpia" module (a dedicated setup for TA experiments). For probing, the remaining 5% of the fundamental pulse at 1030 nm was passed through a mechanical delay stage and focused on a deionised water quevette to create spectrally-broad (approximately from 380 nm to 1.3 μm) pulses. The pump and probe pulses were crossed on the sample's surface and the transmitted probe beam is recorded by a CCD linear Si detector ("Hamamatsu") coupled to a monochromator ("Andor"). The pump beam intensity incident on a sample was estimated as $I_0 = P/\pi f r^2$, where P is the average power of the pump beam, f is the repetition rate, and r is the radius of pump beam spot on the sample measured at $1/e^2$ intensity level of a Gaussian beam profile. The measured beam size was $r = 240 \pm 5$ μm. Such a setup allowed for observation of light-induced absorption changes within the wide spectral range, which can be quantified by wavelength and time-dependent optical density (OD), defined as a ratio of transmitted intensities with pump closed and opened:

$$\Delta OD(t,\lambda) = \lg\left(\frac{I_{no-pump}(\lambda)}{I_{pumped}(t,\lambda)}\right). \tag{1}$$

In the measurements, the detector noise level was accounted for by subtracting the detector readings with all beams blocked. Negative and positive TA signal at given wavelength defined by equation 1 corresponds to induced bleaching or induced absorption, respectively.

For **time-resolved photoluminescence** measurements we used the same laser system with the same beam parameters. The photoluminescence was collected in back-scattering geometry; the scattered pump light was filtered with an optical filter. The PL signal was measured using "Hamamatsu C9300" streak camera with 25 ps time resolution, synchronized with the laser.

Light-induced transient grating measurements were carried out using Nd:YLF PL2243 ("Ekspla") laser, emitting 8 ps duration pulses at 10 Hz repetition rate in 1053 nm fundamental harmonics. The pulses third harmonics at $\lambda_E = 351$ nm and fundamental harmonics at $\lambda_P = 1053$ nm were used for sample excitation and probing, respectively. We note that all investigated samples are transparent to 1053 nm light, which allows for probing of the entire photoexcited depth of a sample. The intensities of incident pump pulses (I_0), transmitted through the sample (I_T), and diffracted (I_D) pulses were monitored by Si photodetectors.

In LITG technique, a spatially-periodical light field is used to excite a sample (hence the diffraction grating), in contrast to a conventional pump-probe where the sample is excited by a beam with a Gaussian profile. Therefore, both carrier recombination and lateral carrier diffusion contribute to LITG signal decay with time[26]. Figure 1 illustrates the creation of transient diffraction grating in a sample. The period of the grating Λ is defined by an angle between the two interfering pump beams Θ and λ_E; the grating period can be varied in an experiment by varying the an-
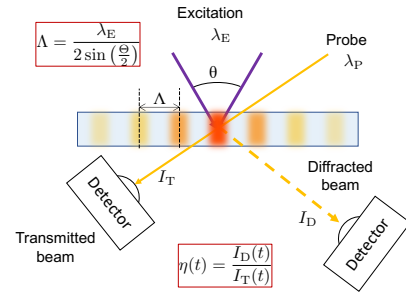

Fig. 1 Illustration of LITG measurement.

gle. In our LITG setup, we use several transmission diffraction gratings (or holographic beam splitters, HBS) with the maximized outputs to ± 1 diffraction orders. HBS splits the pump beam into two coherent parts, which then are projected onto the sample's surface using a $f_1//f_1 + f_2//f_2$ telescope. In this setup, the period of light field on the sample is defined by the period of HBS and magnification of the telescope f_2/f_1.

Periodic light field generates the nonequilibrium carriers with periodic lateral distribution. When probed far from electronic resonances (which is the case in perovskites for 1053 nm probe), the diffraction grating is mainly caused by refractive index modulation by free electron-hole pairs. The probe beam is partially diffracted on this grating, splitting into the "diffracted" and "transmitted" beams. The amplitude of the transient diffraction grating can be characterized using the diffraction efficiency η defined as the ratio of diffracted and transmitted part intensities, $\eta = I_D/I_T$. The decay time constant τ_G of such a grating can be defined as an instantaneous time constant of exponential decay:

$$\eta(t) = \left(\frac{\pi d n_{eh} N(t)}{\lambda_P}\right)^2 = \left(\frac{\pi d n_{eh} N_0}{\lambda_P}\right)^2 \exp\left(-\frac{2t}{\tau_G}\right), \tag{2}$$

here d is the thickness of photoexcited material, n_{eh} – the refractive index change due to a single electron-hole pair, $N(t)$ – the density of carriers at time t, N_0 – the density of photoexcited carriers at the end of the pump pulse, λ_P – the wavelength of probe beam, and τ_G – the decay time constant of transient grating decay. N_0 can be evaluated as $N_0 = \alpha I_0/h\nu$, here α is the absorption coefficient of the sample and $h\nu$ is the pump photon energy.

Figure 2(a) shows the first 150 ps of LITG decay transients recorded in the bulk 3D sample (dots) at three different diffraction grading periods Λ and the corresponding fits to equation 2. Grating decay time τ_G decreases as Λ decreases, due to growing contribution of carrier diffusion to transient grating decay. The partial contributions of carrier lifetime τ and diffusive lifetime τ_D are accounted for by summing the reciprocals:

$$\frac{1}{\tau_G} = \frac{1}{\tau} + \frac{1}{\tau_D} = \frac{1}{\tau} + \frac{4\pi^2 D}{\Lambda^2}, \tag{3}$$

here D is the diffusion coefficient of charge carriers. Equation 3 shows that two material parameters - carrier lifetime and diffusion coefficient - can be obtained from a linear fit of $\tau_G^{-1} = f(\Lambda^{-2})$, as is illustrated in Fig. 2(b). The measurement error for τ and D is defined from standard deviation of the linear fit.
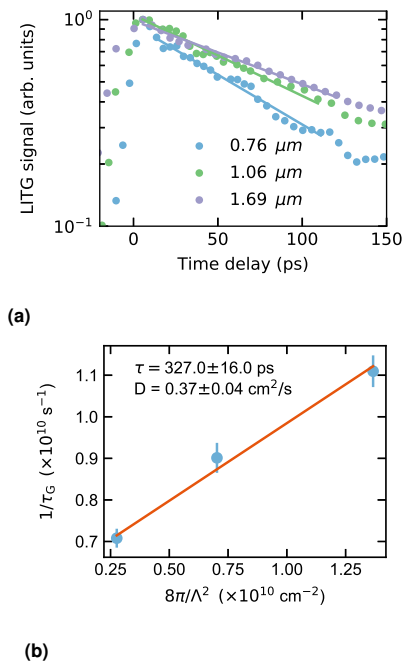
(a)

(b)

Fig. 2 (a) LITG transients recorded at three different grating periods Λ in 3D sample. (b) The dependence of τ_G^{-1} on Λ^{-2} used to extract diffusion coefficient D and carrier lifetime τ, according to equation 3.

We note that for free carriers LITG provides an ambipolar diffusion coefficient D_a, which describes the collective movement of electrons and holes interacting via Dember electric field[26]:

$$D_a = \frac{N_e + N_h}{\left(\dfrac{N_e}{D_h} + \dfrac{N_h}{D_e}\right)}, \qquad (4)$$

here, $N_{e(h)}$ is electron (hole) density, $D_{e(h)}$ - electron (hole) diffusion coefficient. If one type of carriers has significantly smaller diffusivity $D_1 << D_2$, then equation 4 leads to $D_a \approx 2D_1$, provided that both types of carriers are photogenerated in equal carrier densities. Further in the text we omit the subscript and use the notation D, but one has to remember that diffusivity in free carrier plasma is of ambipolar type.

In the analysis of LITG results we make two assumptions. First, we determine D and τ from the initial parts of LITG decay kinetics, within first 100 ps. By doing so, we assume that carrier lifetime is longer than this value and, therefore, the photoexcited carrier density does not deviate much from N_0. This allows for more accurate dependencies on carrier density, in contrast to situation when LITG decay transients are fitted at longer delays. Second, we assume that index changes induced by either electron-hole plasma or excitons are of similar magnitude. To justify this assumption, we refer to the excitonic dielectric function formula derived by D. Chemla and D. Miller[31]:

$$\varepsilon^{-1}(\omega) = \varepsilon_0^{-1}\left[1 + \frac{\Omega^2}{(\omega + i\gamma)^2 - \Delta^2 - \frac{2}{3}\Omega^2}\right] \qquad (5)$$

here ω is the light frequency, ε_0 is the permittivity of a vacuum,

$\Omega^2 = 4\pi Ne^2/\varepsilon_0\mu$ is the frequency that measures exciton density (in turn, N is the particle density and μ is the reduced mass), γ - phenomenological damping constant, and Δ is the energy difference between the ground state and the excited states, which can be roughly approximated by exciton binding energy. Under our experimental conditions, the probe quantum energy is 1.18 eV, while the reported exciton binding energy even in $n = 1$ quasi-2D layers is about 400 meV[32], which allows for approximation $\omega^2 >> \Delta^2$. In such a case, equation 5 becomes similar to the dielectric function of free electron-hole pairs, except for the 2/3 multiplier of Ω in the denominator[31]:

$$\varepsilon^{-1}(\omega) = \varepsilon_0^{-1}\left[1 + \frac{\Omega^2}{(\omega + i\gamma)^2 - \Omega^2}\right]. \qquad (6)$$

3 Results and Discussion

To determine the dependence of diffusion coefficient on photoexcited carrier density $D(N)$, we perform LITG measurements at various excitations in the quasi-2D layers of orders $n = 1 - 4$ as well as in 3D sample; the results are shown in Figure 3.
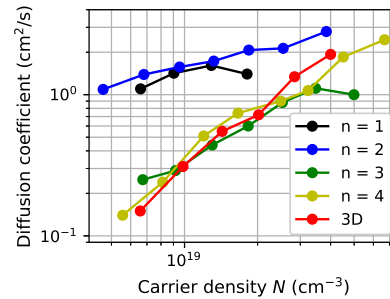

Fig. 3 Ambipolar diffusion coefficient D as a function of photoexcited carrier density ΔN in the $(PEA)_2FA_{n-1}Pb_nBr_{3n+1}$ layers of different order n.

A clear distinction between $n = 1, 2$ and $n \geq 3$ layers can be seen, both for D values and the dependence on carrier density $D(N)$. At low carrier densities (e.g. 5×10^{18} cm^{-3}), D for $n = 1, 2$ samples reaches $0.8 - 0.9$ cm^2/s, while in $n \geq 3$ it is as low as $0.1 - 0.2$ cm^2/s. While $D(N)$ increases with excitation in all samples, the growth rate is considerably faster for $n \geq 3$ layers. Based on our previous model of carrier transport in highly excited perovskites[20,21], one can conclude that diffusion in the thinnest layers experiences smaller influence of carrier localization or trapping if compared to that in the thicker ones. One distinction between these two groups of samples is that in $n = 1, 2$ layers quantum confinement and, thus, exciton binding energy should be much higher; therefore, one could expect that exciton transport prevails in thinner layers, while in the thicker ones a mixture of excitons and free carriers coexist. This assumption is confirmed by time resolved PL and TA measurements, as is discussed further. This implies that exciton diffusion is more efficient due smaller impact of localization. The existence of exciton trapping and related decrease in mobility was indeed confirmed by M. Seitz et al. in $(PEA)_2PbI_4$ 2D perovskite[23]. Higher mobility of excitons in thinner 2D layers also agree with theoretical calculations by S.
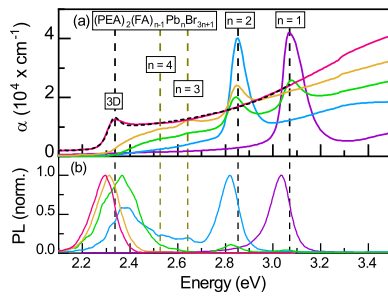
Fig. 4 Spectra of time-integrated absorption (a) and photoluminescense (b) in the $(PEA)_2(FA)_{n-1}Pb_nBr_{3n+1}$ perovskite layers of different dimensions n. Dashed vertical lines mark the positions of excitonic absorption peaks.

Kumavat et al., where carrier mobility in 2D $CH_3NH_3PbI_3$ layer is predicted to be 16 times higher than that in bulk material[33]. On the other hand, the dependence of D on N seen in Fig. 3 is opposite to that reported by S. Deng et al., where a clear increase in D with N was obtained in $(BA)_2(MA)_{n-1}Pb_nI_{3n+1}$[34]. In the latter work it was speculated that dielectric constant increases with thickness of inorganic layer (i.e. with N) increasing screening of Coulomb interaction between the excitons and charged impurities and, thus, decreasing scattering rate. Also, S. Motti et. al. reported 25% lower carrier mobility in 2D $(BA)_2(MA)_{n-1}Pb_nI_{3n+1}$ if compared to 3D perovskite[24]. Comparison of these results suggests that exciton mobility is extremely sensitive to material properties like chemical composition, impurity density, structural etc., and can fluctuate from sample to sample a lot. On the other hand, high D in our samples proves that high diffusivity can be achieved in 2D layers, which is a crucial requirement for devices.

To investigate the potential landscape formed by random formation of different order perovskite sheets in our samples, we measure the stationary absorption and photoluminescence spectra (Figure 4). Comparison of these spectra provides useful information on energy relaxation pathways: while absorption spectra peaks indicate all available electronic states within the investigated spectral region, the PL spectra peaks show the states to which energy relaxation takes place and from where excitons (or free carriers) recombine radiatively. We begin with the absorption spectra of 3D sample, which is typical for a bulk semiconductor. It is composed of partially overlapping excitonic peak and bulk interband absorption band that can be fitted to Elliot model[35]:

$$\alpha(\hbar\omega) \propto \frac{p_{cv}^2}{\hbar\omega}\sqrt{E_{fex}}\left(\sum_s \frac{2E_{fex}}{s^3}\operatorname{sech}\left(\frac{\hbar\omega - E_{fex,s}}{\Gamma}\right) + \right.$$

$$\left. \int_{E_g}^{\infty} \operatorname{sech}\left(\frac{\hbar\omega - E}{\Gamma}\right)\frac{1 + b(E - E_g^{(bulk)})}{1 - e^{-2\pi\sqrt{\frac{E_{fex}}{E - E_g^{(bulk)}}}}}dE \right), \quad (7)$$

here p_{cv} is the interband transition momentum element, E_{fex} - exciton binding energy, $E_{fex,s} = E_g^{(bulk)} - E_{fex}/s^2$ - spectroscopic position of exciton level s, $\Gamma=28$ meV - phonon induced broadening. The fit to this model is shown by the dashed line in Fig. 4(a). The fitting parameters were the bandgap $E_g^{(bulk)} =$

2.378±0.004eV and exciton binding energy $E_{fex} = 45\pm2$ meV. We note that these values are higher than the reported bandgap energy 2.27–2.3 eV[36] and exciton binding energy 22 meV[37], probably due to large spectral broadening of exciton peak at room temperature[35].

While the absorption spectra of thin $n = 1$ and $n = 2$ quasi-2D layers are dominated by a single excitonic peak of corresponding order at 3.07 eV for $n = 1$ or 2.85 eV for $n = 2$, the spectra in thicker layers reveal a mixture of several phases[1]. So, the absorption spectrum of $n = 3$ sample contains a small excitonic peak at 2.65 eV of $n = 3$ layer, together with stronger excitonic contributions from $n = 1$ and $n = 2$ phases. Similarly in $n = 4$ sample, a very small $n = 4$ excitonic peak at 2.53 eV coexists with $n = 3$ and $n = 2$ peaks. Exciton absorption peaks in $n \geq 2$ layers seems to be superimposed with 3D-like interband absorption bands, possibly indicating the existence of 3D perovskite domains. We also note that "native" excitonic peaks in n = 3 and n = 4 samples are much weaker than those of lower order inclusions. The explanation can be two-fold: either the amount of higher order domains exceeds that of lower order domains in these layers, or the exciton population is decreased in higher order domains. The latter is possible if rapid exciton dissociation at abundant domain boundaries is taken into account[38,39]. In addition, the active grain boundaries were also shown to result in strong localization of holes[39], which would contribute to localization-governed $D(N)$ dependence in thicker layers, as discussed above.

The time-integrated PL spectra recorded at low excitation (3.35 $\mu J/cm^2$ at 350 nm) show the energy funnelling from thinner to thicker quasi-2D perovskites. In the $n = 1$ sample, the PL spectrum shows a single excitonic emission peak, red shifted by 38 meV from the absorption peak due to light reabsorption. In the $n = 2$ layer, however, apart from the exciton peak at 2.82 eV a broader band not visible in the absorption spectrum appears at 2.9 eV. Going to even thicker layers, the contribution of exciton luminescence becomes negligible if compared to the broad band at around 2.3 eV. For example, the excitonic peaks at 3.04 eV ($n = 1$), 2.82 eV ($n = 2$), and very weak one at 2.57 eV ($n = 3$) are present in $n = 3$ PL spectra, but they are much smaller than the broad band at 2.3 eV. These facts show that, starting from $n = 2$, quasi-2D samples contain a mixture of phases including higher order or 3D domains and energy relaxation toward lower energy states is rather effective.

To investigate the energy transfer pathways in greater detail, we perform measurements of transient absorption in the layers. TA spectra contain information about occupancy changes in all electronic states, in contrast to PL measurements that observe radiative transitions only. TA setup also provides the best possible time resolution; therefore, it became the established method to study fast excitonic processes in quasi-2D perovskites[15,40]. Figure 5 shows the evolution of differential absorption spectra at low excitations in the quasi-2D samples. In the layers $n = 1$ and $n = 2$, the TA spectra are dominated by single derivative-like features at 3.06 or 2.85 eV, respectively (Figure 5(a, b)). The TA signal of such a shape is typical for excitons in all semiconductors: it is caused by a blue shift of exciton absorption due to multiparticle screening of Coulomb interaction between electrons and
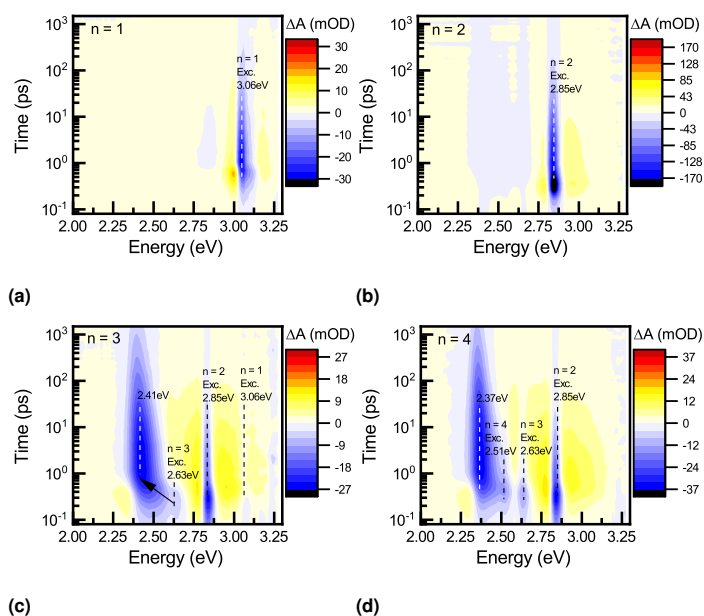
Fig. 5 Colour maps of differential absorption evolution in the quasi-2D layers of different order $n = 1, 2, 3$ and 4 (indicated in the figures) at relatively low excitation $I_0 = 25.5$ μJ/cm^2 by 350 nm laser pulses. Vertical dash lines show the spectral position of exciton absorption in the layers of respective order.

holes[40,41]. In the $n = 1$ sample, no other significantly large signals exist apart from the exciton peak (a short-lived feature at ≈ 2.8 eV is of unclear origin, though its spectral position coincides with the exciton in $n = 2$ layer), which confirms the excitonic nature of carrier dynamics in this layer. Within the first several hundred femtoseconds after photoexcitation, a broadening of this line can be seen, which is presumably due to multiparticle exciton interactions. At delays longer than 1 ps, the broadening disappears and the absorption bleaching dynamics can be described by two-componential decay, with characteristic time constants of 12 ps and 600 ps; exciton dynamics in the $n = 2$ layer is qualitatively similar. The faster component is likely to be caused by fast non-radiative exciton recombination; the presence of such recombination is reflected in low quantum yield of the layers, as is discussed later on.

The TA spectra from thicker $n \geq 3$ layers are composed of multiple components at spectral positions of excitons in domains of different order and of electron hole plasma. Thus, right after the excitation in $n = 3$ layer the exciton components corresponding to $n = 1, 2$ and 3 phases are visible at 3.06, 2.85, and 2.63 eV, respectively. While evolution of two higher energy peaks resembles that in the thinner layers, the exciton at 2.63 eV in $n = 3$ phase exists only up to 1 ps and disappears giving rise to broad and long living band at 2.41 eV (Fig. 5(c)). Similarly, the lowest exciton at 2.51 eV in $n = 4$ evolves into the band at 2.37 eV, although the energy transfer is slower and lasts up to ≈ 10 ps (Fig. 5(d)).

Fast dissociation of excitons in the lowest energy phases rises the question as to the nature of this process. One might consider a possibility that excitons reach the boundaries of domains by lateral in-plain diffusion and dissociate there; however, hav-

ing in mind very short time of these processes this explanation seems unlikely. For instance, $n = 3$ excitons within their lifetime of 1 ps could diffuse only $\sqrt{Dt} = 4.5$ nm, if diffusion coefficient $D = 0.2$ cm^2/s is assumed (see Fig. 3). The typical size of the grains in 2D perovskites have dimensions exceeding micrometer scale[42]. Another possibility is fast carrier movement via ballistic transport, which has been reported in perovskites and other quantum structures[43,44]. However, the ballistic transport occurs on the time scale of hundreds of femtoseconds, but LITG results clearly show the non-ballistic diffusion taking place on much longer timescales of hundreds of picoseconds. Another possible mechanism is that excitons are transferred to neighbouring sheets of higher order and, thus, lower exciton energy via Förster resonance energy transfer[45]. A. Proppe et.al. demonstrated by ultrafast TA measurements and numerical modelling that Förster transfer between sheets is likely as separation between them is only few nanometers (defined by ligand molecule size) and typical timescales for such a process is on tens of femtoseconds scale[15]. Even more, the speed of such a transfer strongly depends on distance between the initial and final states and, thus, on disorder in particular sample (mutual orientation of domains and sheets), which would explain different time scales of exciton dissociation in $n = 3$ and $n = 4$ samples. Such an internal disorder and complex structure of crystallites in 2D perovskites was also confirmed by polarized Raman microspectroscopy[42].

Finally, to understand the nature of the lowest energy spectrally broad TA band, we perform time-resolved photoluminescence measurements. The results are illustrated in Figure 6, where the top row shows the spectra and the bottom row - the temporal traces at PL peak spectral positions, indicated in the figures. Similarly as in absorption measurements, the results can be interpreted in the framework of gradual transition from pure excitonic recombination in $n = 1$ sample to the dominant band-to-band recombination of free electron-hole plasma in the 3D layers. In the $n = 1$ layer, a single peak appears at 3.03 eV and this position does not change with excitation. It has been observed that free excitons in inorganic semiconductors tend to blue shift with excitation due to screening of Coulomb interaction[46]; the absence of such a shift in perovskites has been interpreted as a signature of exciton localization[40]. The PL decay transient recorded at PL peak for $n = 1$ is composed of two components, the fast and slow ones (we note that the fast component in TRPL traces is not the same as the one observed in TA for higher order samples - the latter was by one order of magnitude faster). The dependence of fast component decay time on photoexcited carrier density is shown in Figure 7(a). While the ratio between the amplitudes of fast and slow components changes with excitation, the decay time of the fast one changes only slowly and remains approximately constant for the slower one (340 ± 50 ps). The decay time that is independent on excitation at high densities is typical for excitonic recombination owing to the fact that for excitons the spatial overlap of electron and hole wave functions does not depend on carrier density[47]. Similarly as in the TA transients, the fast decay component represent the onset of fast non-radiative recombination. The behaviour of excitonic peak at 2.82 eV in $n = 2$ is similar, but additional band at 2.35 eV appears; the same band
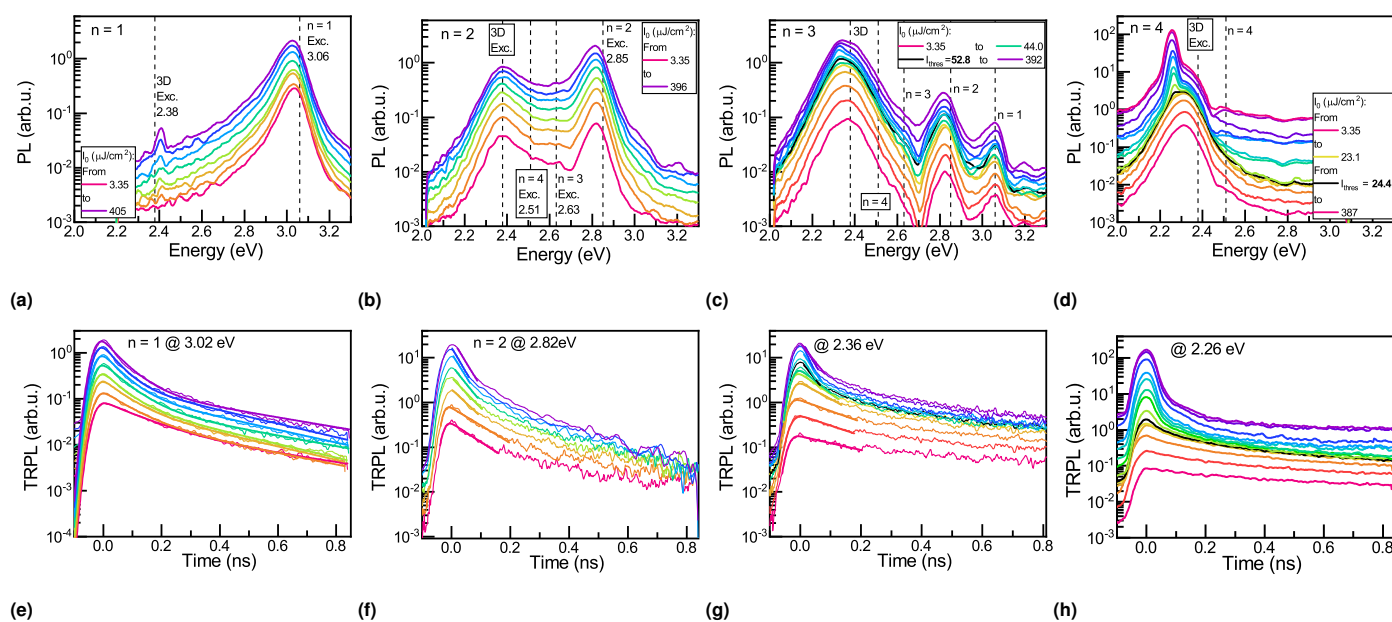
Fig. 6 (a–d) PL spectra integrated within the first nanosecond after excitation and (e–h) temporal traces of PL decay at indicated spectral positions. The curves for different excitations are depicted by different colours as indicated in the legends for each sample.

is also seen in $n = 3$ sample.

A new spectral component of ASE at 2.33 eV emerges in the sample $n = 3$ above the threshold excitation of 52.8 $\mu J/cm^2$ (Fig. 6(c)). ASE is also manifested by appearance of very fast component in the PL transients with decay time shorter than laser pulse duration. No ASE signature was observed for the thinner $n = 1, 2$ layers. The ASE peak appears on the low energy side of the spontaneous PL band and is red shifted with excitation due to band gap renormalization. Red shift of a PL component with carrier density in highly excited semiconductor cannot be explained by excitonic emission, but is rather typical for electron hole plasma and is well known in inorganic semiconductors [48]. Also, the character of fast decay dependence on excitation rapidly changes in the $n = 3$ sample and becomes typical for bimolecular recombination in free carrier plasma. Based on this, we assume that the low energy band that serves as an acceptor for energy funnelling seen in TA spectra (Fig. 5) is caused by free electron-hole plasma rather than excitons. This is feasible having in mind that with the increasing order n the exciton binding energy rapidly drops and at densities as high as in our study (above 5×10^{18} cm^{-3} the Mott density can be reached).

The ASE contribution becomes stronger and the threshold drops to $19 - 20$ $\mu J/cm^2$ in the $n = 4$ and 3D samples, as can be also seen from the quantum yield dependence on excitation, depicted in Figure 7. The increase in the ASE threshold in lower order quasi-2D perovskites is consistent with the results reported for $(PEA)_2MA_{(n-1)}Pb_nI_{3n+1}$ layers [49] and apparently represents fundamental processes in charge dynamics rather than dependence of ASE threshold on the sample thickness (we note that the 3D layer with the lowest ASE threshold was also the thinnest). The ASE threshold dependence in quasi-2D $(PEA)_2Cs_{n-1}Pb_nBr_{3n+1}$ perovskite layers of different order n was investigated by M. Cui et al., where ASE was also observed only for the layers with $n \geq 3$ [50].

The absence of ASE in thinner layers was attributed to the lack of energy transfer to lower energy states, which does not allow for formation of population inversion required for lasing. Our results confirm this conclusions, but we also would like to draw attention to the fact that strong light reabsorption at exciton spectral position drastically increases the ASE threshold and opposes lasing.

It is informative to analyze the decay time of fast component measured at dominant PL peak (it is the excitonic peak in the thin layers and band-to-band recombination band in the thick ones) together with the PL quantum yield at various excitations (Fig. 7(b)). As it was discussed, the decay time constant in the thin ($n = 1, 2$) samples decreases with carrier density only slightly and remain in the range of 50–100 ps for carrier densities from 10^{17} to 10^{19} cm^{-3}, due to excitonic nature of recombination. In contrast, the decay time of free carriers in thicker layers is much higher at low densities (300–500 ps) and decreases roughly linearly with carrier density, confirming the contribution of band-to-band recombination in electron-hole plasma [51]; the sudden drop in lifetime marks the onset of very fast ASE process. However, the noticeably different lifetime in these two groups of samples does not result in significantly different quantum efficiency below the ASE threshold; in contrary, the quantum yield is very similar in all samples. On the other hand, the quantum yield significantly jumps for excitations above the ASE threshold. The presented experimental facts results can be interpreted by the following qualitative picture. In the thinnest layers, carrier dynamics taking place on the time scale of tens and hundreds picoseconds are governed by excitons. They are mobile in the plane of quasi-2D perovskite, but also suffer from efficient nonradiative recombination. It is possible that these two facts also indicate causation, in the sense that faster diffusion coefficient facilitates nonradiative recombination at remote defect sites, e.g. triplet states [9]. In the thicker layers, the diffusivity is small at low carrier densities indi-
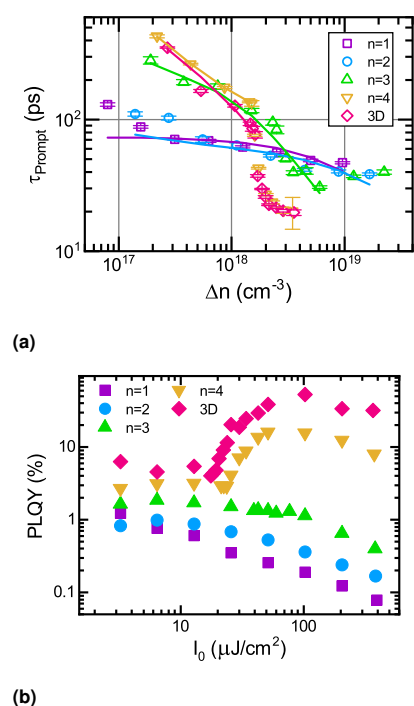
(a)

(b)

Fig. 7 (a) The decay time of the fast PL decay component (see Fig. 6) as a function of photoexcited carrier density. Note that the decay time for $n = 1, 2$ layers represents the decay of excitonic line, while for $n \geq 3$ - decay of electron-hole plasma. (b) Photoluminescence quantum yield as a function of excitation.

cating strong influence of carrier localization. Since the lifetime is much longer but the quantum yield is similar to $n = 1, 2$ layers, it is feasible that both nonradiative and radiative recombination processes are inhibited in $n \geq 3$ samples due to spatial separation of electrons and holes, probably due to action of grain boundaries as suggested by Z. Zhang et. al.[39]. On the other hand, the quantum yield significantly jumps above the ASE threshold, as ASE is very fast radiative process in degenerate electron-hole plasma that overcomes the contribution of slower nonradiative recombination pathways. Our result confirms that fast energy funnelling is essential requirement for ASE to occur in quasi-2D perovskite layers.

4   Conclusions

A concerted application of LITG, TRPL, and TA techniques revealed the energy relaxation pathways of different time scales in highly excited quasi-2D $(PEA)_2FA_{n-1}Pb_nBr_{3n+1}$ layers. In the thinner layers $n = 1$ and 2, we observe diffusion and recombination in excitonic system, while in thicker layers $n \geq 3$ the excitons dissociate due to very fast (<10 ps) energy funnelling to thicker layers where dynamics in electron-hole plasma dominate. We observe no rapid enhancement of diffusion coefficient during the funnelling, which proves that it occurs over small distances only and supports the mechanism of Förster resonance energy transfer between the neighbouring perovskite sheets of different order. In all layers, we observe the growth of diffusivity with excitation, but the growth rate differs in thin and thick samples. We observe significantly higher diffusion coefficient of exciton trans-

port in $n = 1, 2$ order samples: e.g., at lower excitations it exceeds that in thicker samples by roughly one order of magnitude (1 cm^2/s vs 0.1 cm^2/s). The diffusion coefficient dependence on carrier density in $n \geq 3$ layers strongly resembles the carrier transport in bulk perovskites with strong impact of carrier localization/trapping. The observed dependence of diffusion coefficient on layer thickness agrees with theoretical predictions, but is in contrast with some other reports. This discrepancy can stem from different chemical composition of our samples, in agreement with high sensitivity of 2D perovskite transport to structural properties of particular layers. Finally, we show that amplified stimulated emission appears only in electron-hole plasma and not in excitons, presumably due to strong light reabsorption. This illustrates that structural disorder and mixture of different order quasi-2D perovskite layers can be beneficial for light emitting devices.

Conflicts of interest

There are no conflicts to declare.

Acknowledgements

Notes and references

1 R. L. Milot, R. J. Sutton, G. E. Eperon, A. A. Haghighirad, J. Martinez Hardigree, L. Miranda, H. J. Snaith, M. B. Johnston and L. M. Herz, *Nano Letters*, 2016, **16**, 7001–7007.

2 Y. Chen, Y. Sun, J. Peng, J. Tang, K. Zheng and Z. Liang, *Advanced Materials*, 2018, **30**, 1703487.

3 T. C. Sum, M. Righetto and S. S. Lim, *The Journal of Chemical Physics*, 2020, **152**, 130901.

4 I. C. Smith, E. T. Hoke, D. Solis-Ibarra, M. D. McGehee and H. I. Karunadasa, *Angewandte Chemie*, 2014, **126**, 11414–11417.

5 D. H. Cao, C. C. Stoumpos, O. K. Farha, J. T. Hupp and M. G. Kanatzidis, *Journal of the American Chemical Society*, 2015, **137**, 7843–7850.

6 T. Zhou, M. Wang, Z. Zang, X. Tang and L. Fang, *Solar Energy Materials and Solar Cells*, 2019, **191**, 33–38.

7 H. Tsai, W. Nie, J.-C. Blancon, C. C. Stoumpos, R. Asadpour, B. Harutyunyan, A. J. Neukirch, R. Verduzco, J. J. Crochet, S. Tretiak, L. Pedesseau, J. Even, M. A. Alam, G. Gupta, J. Lou, P. M. Ajayan, M. J. Bedzyk, M. G. Kanatzidis and A. D. Mohite, *Nature*, 2016, **536**, 312–316.

8 R. Yang, R. Li, Y. Cao, Y. Wei, Y. Miao, W. L. Tan, X. Jiao, H. Chen, L. Zhang, Q. Chen, H. Zhang, W. Zou, Y. Wang, M. Yang, C. Yi, N. Wang, F. Gao, C. R. McNeill, T. Qin, J. Wang and W. Huang, *Advanced Materials*, 2018, **30**, 1804771.

9 C. Qin, A. S. D. Sandanayaka, C. Zhao, T. Matsushima, D. Zhang, T. Fujihara and C. Adachi, *Nature*, 2020, **585**, 53–57.

10 K. Tanaka, T. Takahashi, T. Kondo, T. Umebayashi, K. Asai and K. Ema, *Physical Review B*, 2005, **71**, 045312.

11 D. B. Straus and C. R. Kagan, *The Journal of Physical Chemistry Letters*, 2018, **9**, 1434–1447.

12 D. Marongiu, M. Saba, F. Quochi, A. Mura and G. Bongiovanni, *Journal of Materials Chemistry C*, 2019, **7**, 12006–12018.

13 L. N. Quan, M. Yuan, R. Comin, O. Voznyy, E. M. Beauregard, S. Hoogland, A. Buin, A. R. Kirmani, K. Zhao, A. Amassian, D. H. Kim and E. H. Sargent, *Journal of the American Chemical Society*, 2016, **138**, 2649–2655.

14 M. Yuan, L. N. Quan, R. Comin, G. Walters, R. Sabatini, O. Voznyy, S. Hoogland, Y. Zhao, E. M. Beauregard, P. Kanjanaboos, Z. Lu, D. H. Kim and E. H. Sargent, *Nature Nanotechnology*, 2016, **11**, 872–877.

15 A. H. Proppe, M. H. Elkins, O. Voznyy, R. D. Pensack, F. Zapata, L. V. Besteiro, L. N. Quan, R. Quintero-Bermudez, P. Todorovic, S. O. Kelley, A. O. Govorov, S. K. Gray, I. Infante, E. H. Sargent and G. D. Scholes, *The Journal of Physical Chemistry Letters*, 2019, **10**, 419–426.

16 M. Wang, H. Wang, W. Li, X. Hu, K. Sun and Z. Zang, *Journal of Materials Chemistry A*, 2019, **7**, 26421–26428.

17 M. Wang, W. Li, H. Wang, K. Yang, X. Hu, K. Sun, S. Lu and Z. Zang, *Advanced Electronic Materials*, 2020, **6**, 2000604.

18 L. M. Herz, *ACS Energy Letters*, 2017, **2**, 1539–1548.

19 J. Bisquert, *Physical Chemistry Chemical Physics*, 2008, **10**, 3175.

20 P. Ščajev, R. Aleksiejūnas, S. Miasojedovas, S. Nargelas, M. Inoue, C. Qin, T. Matsushima, C. Adachi and S. Juršėnas, *The Journal of Physical Chemistry C*, 2017, **121**, 21600–21609.

21 P. Ščajev, C. Qin, R. Aleksiejūnas, P. Baronas, S. Miasojedovas, T. Fujihara, T. Matsushima, C. Adachi and S. Juršėnas, *The Journal of Physical Chemistry Letters*, 2018, **9**, 3167–3172.

22 C. Zhou, W. Chen, S. Yang, Q. Ou, Z. Gan, Q. Bao, B. Jia and X. Wen, *ACS Applied Materials & Interfaces*, 2020, **12**, 26384–26390.

23 M. Seitz, A. J. Magdaleno, N. Alcázar-Cano, M. Meléndez, T. J. Lubbers, S. W. Walraven, S. Pakdel, E. Prada, R. Delgado-Buscalioni and F. Prins, *Nature Communications*, 2020, **11**, 2035.

24 S. G. Motti, T. Crothers, R. Yang, Y. Cao, R. Li, M. B. Johnston, J. Wang and L. M. Herz, *Nano Letters*, 2019, **19**, 3953–3960.

25 X. Yang, X. Zhang, J. Deng, Z. Chu, Q. Jiang, J. Meng, P. Wang, L. Zhang, Z. Yin and J. You, *Nature Communications*, 2018, **9**, 570.

26 H. J. Eichler, P. Gunter and D. W. Pohl, *Laser-Induced Dynamic Grattings*, Springer-Verlag, New York, 1986.

27 D. Webber, C. Clegg, A. W. Mason, S. A. March, I. G. Hill and K. C. Hall, *Applied Physics Letters*, 2017, **111**, 121905.

28 D. H. Arias, D. T. Moore, J. van de Lagemaat and J. C. Johnson, *The Journal of Physical Chemistry Letters*, 2018, **9**, 5710–5717.

29 P. Ščajev, D. Litvinas, V. Soriūtè, G. Kreiza, S. Stanionytè and S. Juršėnas, *The Journal of Physical Chemistry C*, 2019, **123**, 23838–23844.

30 P. Ščajev, R. Aleksiejūnas, P. Baronas, D. Litvinas, M. Kolenda, C. Qin, T. Fujihara, T. Matsushima, C. Adachi and S. Juršėnas, *The Journal of Physical Chemistry C*, 2019, **123**, 19275–19281.

31 D. S. Chemla and D. A. B. Miller, *Journal of the Optical Society of America B*, 1985, **2**, 1155.

32 J. V. Passarelli, C. M. Mauck, S. W. Winslow, C. F. Perkinson, J. C. Bard, H. Sai, K. W. Williams, A. Narayanan, D. J. Fairfield, M. P. Hendricks, W. A. Tisdale and S. I. Stupp, *Nature Chemistry*, 2020, **12**, 672–682.

33 S. R. Kumavat, Y. Sonvane, D. Singh and S. K. Gupta, *The Journal of Physical Chemistry C*, 2019, **123**, 5231–5239.

34 S. Deng, E. Shi, L. Yuan, L. Jin, L. Dou and L. Huang, *Nature Communications*, 2020, **11**, 664.

35 N. Sestu, M. Cadelano, V. Sarritzu, F. Chen, D. Marongiu, R. Piras, M. Mainas, F. Quochi, M. Saba, A. Mura and G. Bongiovanni, *The Journal of Physical Chemistry Letters*, 2015, **6**, 4566–4572.

36 G. Mannino, I. Deretzis, E. Smecca, A. La Magna, A. Alberti, D. Ceratti and D. Cahen, *The Journal of Physical Chemistry Letters*, 2020, **11**, 2490–2496.

37 K. Galkowski, A. Mitioglu, A. Miyata, P. Plochocka, O. Portugall, G. E. Eperon, J. Tse-Wei Wang, T. Stergiopoulos, S. D. Stranks, H. J. Snaith and R. J. Nicholas, *Energy & Environmental Science*, 2016, **9**, 962–970.

38 J.-C. Blancon, H. Tsai, W. Nie, C. C. Stoumpos, L. Pedesseau, C. Katan, M. Kepenekian, C. M. M. Soe, K. Appavoo, M. Y. Sfeir, S. Tretiak, P. M. Ajayan, M. G. Kanatzidis, J. Even, J. J. Crochet and A. D. Mohite, *Science*, 2017, **355**, 1288–1292.

39 Z. Zhang, W.-H. Fang, R. Long and O. V. Prezhdo, *Journal of the American Chemical Society*, 2019, **141**, 15557–15566.

40 X. Wu and M. T. Trinh, *J. Phys. Chem. C*, 2015, **119**, 14714–14721.

41 N. Peyghambarian, H. M. Gibbs, J. L. Jewell, A. Antonetti, A. Migus, D. Hulin and A. Mysyrowicz, *Physical Review Letters*, 1984, **53**, 2433–2436.

42 S. Toda, N. Yanagita, E. Jokar, E. W.-G. Diau and S. Shigeto, *The Journal of Physical Chemistry Letters*, 2020, **11**, 3871–3876.

43 J. Sung, C. Schnedermann, L. Ni, A. Sadhanala, R. Y. S. Chen, C. Cho, L. Priest, J. M. Lim, H.-K. Kim, B. Monserrat, P. Kukura and A. Rao, *Nature Physics*, 2020, **16**, 171–176.

44 P. Gong, Y.-Y. Yang, W.-D. Ma, X.-Y. Fang, X.-L. Jing, Y.-H. Jia and M.-S. Cao, *Physica E: Low-dimensional Systems and Nanostructures*, 2021, **128**, 114578.

45 L. Lei, D. Seyitliyev, S. Stuard, J. Mendes, Q. Dong, X. Fu, Y.-A. Chen, S. He, X. Yi, L. Zhu, C.-H. Chang, H. Ade, K. Gundogdu and F. So, *Advanced Materials*, 2020, **32**, 1906571.

46 S. Wachter, M. Maute, H. Kalt, I. Galbraith, C. Sieh, T. Meier and S. W. Koch, *Physica B: Condensed Matter*, 2002, **314**, 309–313.

47 W. Liu, R. Butté, A. Dussaigne, N. Grandjean, B. Deveaud and G. Jacopin, *Physical Review B*, 2016, **94**, 195411.

48 G. Tränkle, E. Lach, A. Forchel, F. Scholz, C. Ell, H. Haug, G. Weimann, G. Griffiths, H. Kroemer and S. Subbanna, *Physical Review B*, 1987, **36**, 6712–6714.

49 R. M. Leyden, T. Matsushima, C. Qin, S. Ruan, H. Ye and C. Adachi, *Physical Chemistry Chemical Physics*, 2018, **20**, 15030–15036.

50 M. Cui, C. Qin, Y. Jiang, M. Yuan, L. Xu, D. Song, Y. Jiang and Y. Liu, *The Journal of Physical Chemistry Letters*, 2020, **11**, 5734–5740.

51 L. H. Manger, M. B. Rowley, Y. Fu, A. K. Foote, M. T. Rea, S. L. Wood, S. Jin, J. C. Wright and R. H. Goldsmith, *The Journal of Physical Chemistry C*, 2017, **121**, 1062–1071.